The Astronomical Journal, 161:266 (14pp), 2021 June https://doi.org/10.3847/1538-3881/abdf4d

Terminus: A Versatile Simulator for Space-based Telescopes

Billy Edwards[1,2] and Ian Stotesbury[1]
[1] Blue Skies Space Ltd., 69 Wilson Street, London, EC2A 2BB, UK; billy@bssl.space
[2] Department of Physics and Astronomy, University College London, Gower Street, London, WC1E 6BT, UK
Received 2020 August 7; revised 2021 January 4; accepted 2021 January 20; published 2021 May 14

Abstract

Space-based telescopes offer unparalleled opportunities for characterizing exoplanets, solar system bodies, and stellar objects. However, observatories in low-Earth orbits (e.g., Hubble, CHaracterising ExOPlanets Satellite, Twinkle, and an ever-increasing number of cubesats) cannot always be continuously pointed at a target due to Earth obscuration. For exoplanet observations consisting of transit, or eclipse, spectroscopy, this causes gaps in the light curve, which reduces the information content and can diminish the science return of the observation. Terminus, a time-domain simulator, has been developed to model the occurrence of these gaps to predict the potential impact on future observations. The simulator is capable of radiometrically modeling exoplanet observations as well as producing light curves and spectra. Here, Terminus is baselined on the Twinkle mission, but the model can be adapted for any space-based telescope and is especially applicable to those in a low-Earth orbit. Terminus also has the capability to model observations of other targets such as asteroids or brown dwarfs.

Unified Astronomy Thesaurus concepts: Exoplanet atmospheres (487); Space telescopes (1547); Asteroids (72); Astronomical instrumentation (799); Infrared telescopes (794)

1. Introduction

To date, several thousand extrasolar planets have been discovered. With many of these now being detected around bright stars, and with many more to come from missions such as the Transiting Exoplanet Survey Satellite (Ricker et al. 2014; Barclay et al. 2018), the characterization of these worlds has begun and will accelerate over the next decade. Ground-based instruments have detected absorption and emission lines in exoplanet atmospheres via high-resolution spectra (e.g., Hoeijmakers et al. 2018; Ehrenreich et al. 2020), while the Hubble and Spitzer space telescopes have used lower-resolution spectroscopy or photometry to probe the chemical abundances and thermal properties of tens of planets (e.g., Iyer et al. 2016; Sing et al. 2016; Tsiaras et al. 2018; Garhart et al. 2020).

In the coming years, several missions, some of which are specifically designed for exoplanet research, will be launched to provide further characterization. While the James Webb Space Telescope (JWST; Greene et al. 2016) and Ariel (Tinetti et al. 2018; Tinetti et al. 2021) will be located at L2, observatories such as the CHaracterising ExOPlanets Satellite (CHEOPS; Benz et al. 2021), which was launched in 2019 December, and Twinkle (Edwards et al. 2019c) will operate from a low-Earth orbit and as such will have to contend with Earth obscuration.

The orbit will cause gaps in some of the observations obtained by these missions, which will impact their information content due to parts of the transit light curve being missed, decreasing the precision of the recovered transit parameters. Additionally, the thermal environment of a low-Earth orbit and the breaks in observing can lead to recurring systematic trends such as ramps in the recorded flux due to thermal breathing of the telescope and detector persistence. Such gaps and systematics are experienced in all exoplanet observations with Hubble (e.g., Deming et al. 2013; Kreidberg et al. 2014). It should be noted, however, that Hubble is situated in an equatorial orbit, which is significantly different from the Sun-synchronous orbits of CHEOPS and Twinkle. Sun-synchronous orbits allow for certain areas of the sky, specifically those in the anti-Sun direction, to be observed for longer periods without interruption. Additionally, the thermal environment is more stable due to the smaller variations in the spacecraft–Earth–Sun geometry. Previous missions to have operated in Sun-synchronous orbits include the Convection, Rotation and planetary Transits (CoRoT, Bordé et al. 2003), Akari (Murakami et al. 2007), and WISE/NEOWISE (Wright et al. 2010; Mainzer et al. 2014). Due to its Earth-trailing orbit, Spitzer (Werner et al. 2004) did not experience gaps in its observations.

When designing future instrumentation, understanding the expected performance for the envisioned science cases is paramount. Static models, often referred to as radiometric or sensitivity models, are suitable for studying the instrument performance over a wide parameter space (i.e., for many different targets) as they are generally quick to run and require relatively minimal information about the instrumentation. Radiometric models are a useful way to understand the capabilities of upcoming exoplanet observatories and have been widely used. The ESA Radiometric Model (ERM; Puig et al. 2015) was used to simulate the performance of the ESA M3 candidate Exoplanet Characterisation Observatory (EChO; Tinetti et al. 2012) and was subsequently used for Ariel (Puig et al. 2018). A newer, Python-based version, ArielRad, was recently developed (Mugnai et al. 2020), while PandExo has been created for simulating exoplanet observations with Hubble and JWST (Batalha et al. 2017), and the NIRSpec Exoplanet Exposure Time Calculator was built specifically for modeling transit and eclipse spectroscopy with JWST's NIRSpec instrument (Nielsen et al. 2016). These usually account for the efficiency of the optics and simple noise contributions such as photon, dark current, readout, and instrument/telescope emission.

More complex effects, such as jitter, stellar variability and spots, and correlated noise sources require models that have a time-domain aspect. These tools usually also produce simulated detector images that can act as realistic data products for the mission, accounting for detector effects such as correlated noise between pixels or inter- and intrapixel variations. For example,

ExoSim is a numerical end-to-end simulator of transit spectroscopy currently being utilized for the Ariel mission (Pascale et al. 2015; Sarkar et al. 2016, 2017). The tool has been created to explore a variety of signal and noise issues that occur in, and may bias, transit spectroscopy observations, including instrument systematics and the other effects previously mentioned. By producing realistic raw data products, the outputs can also be fed into data reduction pipelines to explore, and remove, potential biases within them as well as develop new reduction and data correction methods. End-to-end simulators such as ExoSim are therefore powerful tools for understanding the capabilities of an instrument design. Additional time-domain simulators of note include ExoNoodle (Martin-Lagarde et al. 2021), which utilizes MIRISim (Geers et al. 2019) to model time series with the JWST MIRI instrument; Wayne, which models Hubble spatial scans of exoplanets (Varley et al. 2017); and the simulators developed for the CHEOPS and Colorado Ultraviolet Transit Experiment missions (Sreejith et al. 2019; Futyan et al. 2020). While the complexity of these types of tools can be hugely advantageous in understanding intricate effects, it can also be their biggest weakness; such sophisticated models require a great deal of time to develop and run as well as an excellent understanding of all parts of the instrument design. They can therefore only be applied to highly refined designs and run for a small number of cases. The solution to the issue of complexity versus efficiency is to use both types of models. For Ariel, ExoSim is used to validate the outcomes of ArielRad for selected, representative targets. ArielRad is then used as the workhorse for modeling the capability of thousands of targets due to its superior speed (Edwards et al. 2019b; Mugnai et al. 2020).

Here, we describe the Terminus tool, which has been developed to model transit (and eclipse) observations with Twinkle, to explore the impact of Earth obscuration, and to allow for efficient scheduling methods to be developed to minimize this impact. The simulator, however, is not mission specific and could be adapted for other observatories, with a particular applicability for satellites in low-Earth orbit.

The Twinkle Space Mission[3] is a new, fast-track satellite designed to begin science operations in 2024. It has been conceived for providing faster access to spectroscopic data from exoplanet atmospheres and solar system bodies. Twinkle is equipped with a visible and infrared spectrometer, which simultaneously covers 0.5–4.5 μm with a resolving power of $R \sim 20$–70 across this range. Twinkle has been designed with a telescope aperture of 0.45 m. Twinkle's field of regard is a cone with an opening angle of 40°, centered on the anti-Sun vector (Savini et al. 2018).

Previously, the ESA Radiometric Model (ERM; Puig et al. 2015, 2018), which assumes full light curves are observed, has been used to model the capabilities of Twinkle (see Edwards et al. 2019c). Terminus includes a radiometric model, built upon the concepts of the ERM, but it has been upgraded to also have the capacity to simulate light curves. The code also contains the ability to model the orbit of a spacecraft, thus allowing for the availability of targets to be understood given solar, lunar, and Earth exclusion angles. The capability to model these gaps is not available in other tools such as ArielRad or ExoSim and is one of the driving factors behind the creation of Terminus. Additionally, the Twinkle mission will not be limited to exoplanet characterization and will also observe solar system bodies, brown dwarfs, and other astrophysical objects. As such, Terminus builds upon the work of Edwards et al. (2019a, 2019d) and can be used to calculate the predicted data quality and observational periods for these objects, another feature that is not present in other similar codes.

In this work, we first describe the portion of the simulator that calculates the target signal and noise contributions before comparing the outputs of simulated light-curve fitting to radiometric estimates. Next, the orbital module is detailed and validated against outputs from an orbital dynamics software. Using this, we explore the effect of gaps for observations of HD 209458 b and WASP-127 b with Twinkle. Finally, we discuss Twinkle's ability to observe asteroids by focusing on potential observations of the Near-Earth Object (NEO) 99942 Apophis (2004 MN4).

2. Simulator Structure

Terminus has been constructed in Python and has several different stages. It can be operated as a simple radiometric model, used to calculate the expected signal-to-noise ratio (S/N) on a given number of atmospheric scale heights, or be utilized to create simulated light curves. An instrument file is loaded (which includes parameters such as telescope aperture, quantum efficiency, etc.) and the star flux on the detector calculated. Point spread functions (PSFs) can be imported from external sources. In Sections 2.1–2.4, we discuss the structure of the simulator and an overview is given in Figure 1.

2.1. Target Parameters

A catalog of planets has been created following the methodology of Edwards et al. (2019b), and data are taken from the NASA Exoplanet Archive (Akeson et al. 2013).

2.2. Radiometric Model

The stellar flux at Earth is calculated using spectral energy distributions (SEDs) from the PHOENIX BT-Settl models by Allard et al. (2012), Husser et al. (2013), and Baraffe et al. (2015). The spectral irradiance from a host star at the aperture of the telescope is given by

$$E_S(\lambda) = S_S(\lambda)\left(\frac{R_*}{d}\right)^2, \quad (1)$$

where $S_S(\lambda)$ is the star spectral irradiance from the Phoenix catalog (W m^{-2} μm^{-1}) and d is the distance to the star. The effective collecting area of the telescope is then accounted for before the flux is integrated into the spectral bins of the instrumentation to give a photon flux per bin. The signal is then propagated through the instrument to the detector focal planes, taking into account the transmission of each optical component and diffracting element as well as the quantum efficiency of the detector. The final signal, in electrons per second, from the star in each spectral bin is determined as a 1D flux rate before being convolved with 2D PSFs and the instrument dispersion to create a detector image. The detector image, like the one shown in Figure 2, is utilized to calculate the saturation time for the target while the 1D flux rate is used for all other calculations. A variety of sources of noise are accounted for in each of the models. In addition to photon noise, the simulator calculates

[3] http://www.twinkle-spacemission.co.uk

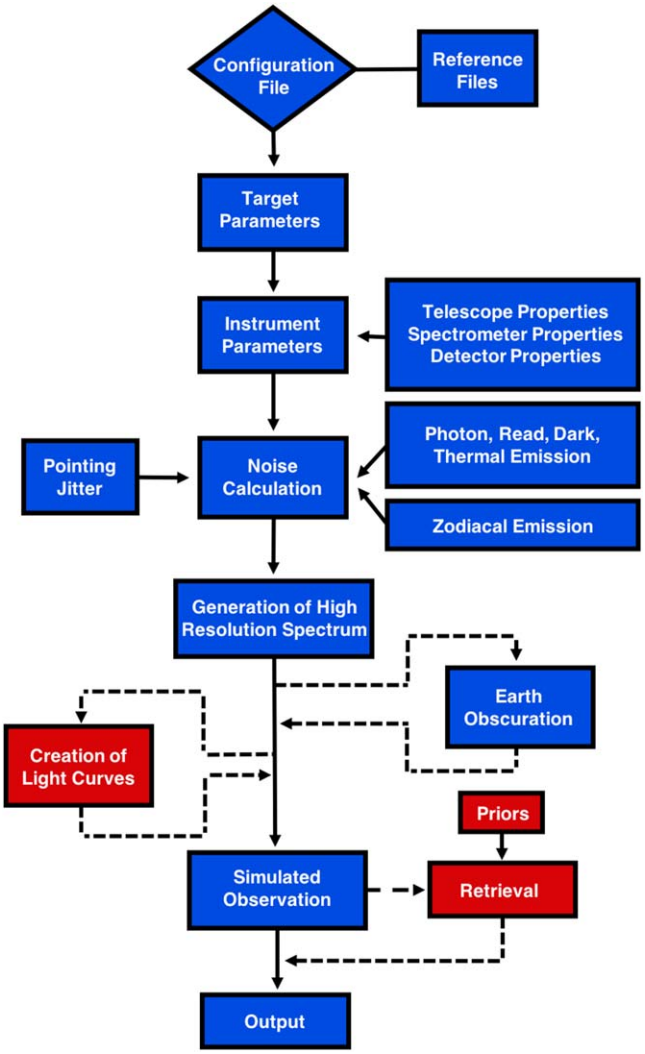

Figure 1. Overview of the simulator structure. Generic parts are represented by blue shapes while red indicates functions that are exoplanet specific. Dotted lines indicate portions that are not compulsory.

the contributions from dark current, instrument and telescope emission, zodiacal background emission, and readout noise. Additionally, photometric uncertainties due to spacecraft jitter can be imported and interpolated from time-domain simulators such as ExoSim (see Section 2.2.3). Some of these noise sources are wavelength dependent (e.g., zodiacal background) while others are not (e.g., read noise).

2.2.1. Calculating Noise per Exposure

In describing the acquisition of data, we use the nomenclature of Rauscher et al. (2007) in which a frame refers to the clocking and digitization of pixels within a specified area of the detector known as a subarray. The size of the subarray dictates the time required for it to read out. Here, given the footprint of Twinkle's spectrometer on the detector, we assume a fastest frame time of 0.5 s, which is similar to that for the 1024A subarray on JWST NIRSpec (0.45 s; Pontoppidan et al. 2016). A collection of frames then forms a group although here; as with the JWST time series, the number of frames is set to one (i.e., $t_g = t_f$). A collection of nondestructively read groups, along with a detector reset, forms an integration. Here, the

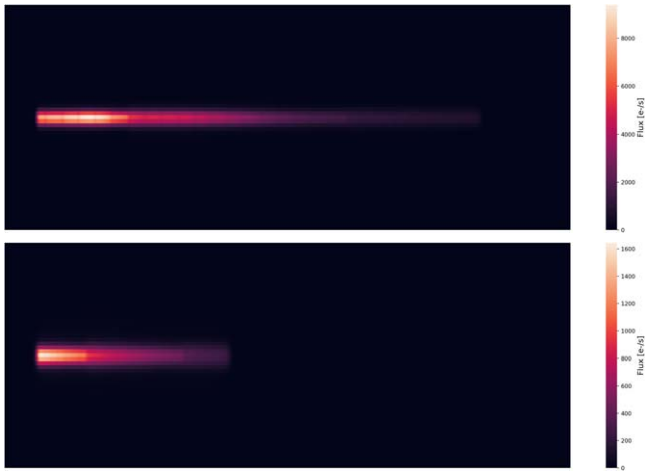

Figure 2. Example detector images generated by Terminus for Twinkle Ch0 (top) and Ch1 (bottom). These are used purely for the calculation of the saturation time for each target.

detector reset time after a destructive read is also assumed to be equivalent to the frame time. As the duration of a transit/eclipse is generally orders of magnitude longer than the saturation time of the detector, many integrations will be taken during an observation. The total noise variance per integration, $\sigma^2_{\rm exp}$, is given by

$$\sigma^2_{\rm exp} = \frac{12(n_g - 1)}{n_g(n_g + 1)} n_{\rm pix}\sigma^2_{\rm read} + \frac{6(n_g^2 + 1)}{5n_g(n_g + 1)} \times (n_g - 1)t_g i_{\rm total} \quad (2)$$

from Rauscher et al. (2007), where $n_{\rm g}$ is the number of groups (nondestructive reads) per exposure, $\sigma_{\rm read}$ is the read noise in e^-/pix rms, $n_{\rm pix}$ is the number of pixels in the spectral bin, $t_{\rm g}$ is the time for a single nondestructive group read, and $i_{\rm total}$ is the total flux in e^-/s. For JWST observations, the standard practice for exoplanet observations is to maximize the number of groups (Batalha et al. 2017). Meanwhile, Ariel will use a variety of readout modes, depending upon the brightness of the target, with correlated double sampling (CDS; $n_{\rm g} = 2$) for brighter sources targets and multiple up-the-ramp reads for fainter targets (Focardi et al. 2018). Collecting several up-the-ramp reads can be useful in correcting for cosmic-ray impacts while also reducing the read noise. Additional reads, however, increase the photon noise contribution and thus Terminus varies the number of up-the-ramp reads according to the brightness of the target to attempt to optimize noise. In each case, the maximum number of up-the-ramp reads is calculated and Equation (2) used to selected the number of reads that yields the lowest noise per transit observation (using Equations (2)–(7)). $n_{\rm pix}$ can be selected by specifying a required encircled energy but when importing jitter simulations from ExoSim, $n_{\rm pix}$ is set to the values used in these simulations as outlined in Section 2.2.3. In Equation (2), $i_{\rm total}$ is defined as

$$i_{\rm total} = i_{\rm sig} + n_{\rm pix}(i_{\rm dark} + i_{\rm bdg}), \quad (3)$$

where $i_{\rm sig}$ is the total signal from the star in the spectral bin (e^-/s), while $i_{\rm dark}$ and $i_{\rm bdg}$ are the dark current and background signals, respectively (in e^-/s/pix). Currently, $i_{\rm bdg}$ is assumed to be from the emission of optical elements and zodiacal

emission, as detailed in Section 2.2.2, but future updates will include contributions from nearby stars. For exoplanet spectroscopy, the total observational time is generally quantized in terms of the duration of a transit/eclipse event, T. The model assumes the time spent during ingress (T_{12}) and egress (T_{34}) is negligible compared to the primary transit time (T_{23}) and thus $T = T_{23} = T_{14}$. The transit time can be calculated from

$$T_{14} = \sqrt{1 - b^2}\,\frac{R_* P}{\pi a} \tag{4}$$

for a given system, where P is the orbital period. The fractional noise on the star signal over one transit duration is then given by

$$\sigma_{\rm Star} = \frac{1}{\sqrt{n_{\rm int}}}\frac{\sigma_{\rm exp}}{i_{\rm sig}}, \tag{5}$$

where $n_{\rm int}$ is the number of integrations over one transit duration, which is calculated from

$$n_{\rm int} = \frac{T_{14}}{t_r + t_g n_g}, \tag{6}$$

where $t_{\rm r}$ is the time taken to reset the detector. As a baseline, we take $t_{\rm r}$ to be equivalent to the frame time, $t_{\rm f}$ (0.5 s). As noted by Batalha et al. (2017), if $t_{\rm g} = t_{\rm r} = t_{\rm f}$, then the duty cycle (i.e., the efficiency) is given by $(n_{\rm g} - 1)/(n_{\rm g} + 1)$.

The measurement of the transit depth is differential, and thus, the error (i.e., the 1σ uncertainty) on the transit depth is given by

$$\sigma_{TD} = \sigma_{\rm Star}\sqrt{1 + \frac{1}{n_{T_{14}}}}, \tag{7}$$

where $n_{T_{14}}$ is the number of transit durations observed out of transit (i.e., the baseline). For all simulations presented here, $n_{T_{14}}$ is set to 2 (i.e., $1 \times T_{14}$ is spent both before/after the main observation). The error is calculated in this way for every spectral bin.

2.2.2. Zodiacal Emission

We calculate the contribution of zodiacal emission using the prescription from Pascale et al. (2015) and Sarkar et al. (2020a). The signal is composed of two blackbodies, with associated coefficients, to model the reflected and emitted components. The spectral brightness is given by

$$\begin{aligned}{\rm Zodi}(\lambda) = \beta(&3.5 \times 10^{-14} B_\lambda(5500\ {\rm K}) \\ &+ 3.58 \times 10^{-8} B_\lambda(270\ {\rm K})),\end{aligned} \tag{8}$$

where the coefficient β modifies the intensity of the zodiacal light based upon the decl. of the target. At the ecliptic poles, $\beta = 1$ provides a good fit to the intensity shown in Leinert et al. (1998). Sarkar et al. (2020a) fitted a polynomial to data from this study, along with zodiacal intensities from James et al. (1997), Tsumura et al. (2010), to provide a measure of the increase in intensity at different latitudes. If d is the ecliptic latitude, then the coefficient is given by

$$\begin{aligned}\beta = &-0.22968868\zeta^7 + 1.12162927\zeta^6 - 1.72338015\zeta^5 \\ &+ 1.13119022\zeta^4 - 0.95684987\zeta^3 + 0.2199208\zeta^2 \\ &- 0.05989941\zeta + 2.57035947,\end{aligned} \tag{9}$$

where $\zeta = \log_{10}(d + 1)$. This relation falls below 1 at $d = 57.^\circ355$, and so β is fixed to 1 for latitudes greater than this (Sarkar et al. 2020a).

2.2.3. Pointing Jitter

Directly modeling uncertainties due to spacecraft jitter is beyond the capabilities of Terminus. Hence, ExoSim has been adapted to the Twinkle design to study the effects of pointing jitter on science performance. ExoSim, first conceived for EChO (Pascale et al. 2015) and now used for the Ariel mission, has previously been adapted for simulating observations with JWST (Sarkar et al. 2020a) and the EXoplanet Climate Infrared TElescope (EXCITE; Tucker et al. 2018; Nagler et al. 2019). The modified version, christened TwinkleSim, was run for a number of stellar types ($T_{\rm S} = 3000$, 5000, 6100 K) and magnitudes ($K_{\rm S} = 6$, 9, 12), and the uncertainty due to jitter determined in each case. Twinkle's baseline pointing solution is based upon a high-performance gyroscope and a power spectral density (PSD) was supplied by the engineering team at the satellite manufacturer, Airbus. For each simulation, a variety of different extraction apertures were trialed with larger apertures, reducing the jitter by ensuring clipping did not occur but increasing the noise from other sources due to sampling more pixels (e.g., dark current). After trialing a number of solutions, the aperture was set to be rectangular with a width of 2.44 times the width of the Airy disk at the longest wavelength of each channel. In terms of pixels, this is equivalent to 12 and 22 in the spatial direction, for Ch0 and Ch1, respectively, while the spectral pixels per bin are set to 6 and 7.

When combining observations, time-correlated noise may integrate down more slowly than uncorrelated noise, which is assumed to decrease with the square root of the number of observations, and thus can contribute more heavily to the final noise budget. To account for these Allan deviations. plots were produced using TwinkleSim. A power-law trend can be fitted to this and used to derive a wavelength-dependent fractional noise term that jitter induces on the photon noise. For more details on this process, we refer the reader to Sarkar et al. (2020a).

2.2.4. Transit Signal

During transit, the critical signal is the fraction of stellar light that passes through the atmosphere of the exoplanet. This signal is determined by the ratio of the projected area of the atmosphere to that of the stellar disk and thus is given by

$$\frac{2R_p \Delta z(\lambda)}{R_*^2}, \tag{10}$$

where Δz is the height of the atmosphere. The size of the atmosphere is taken to be equivalent to the height above the 10 bar radius, at which point the atmosphere is assumed to be opaque. The pressure of an atmosphere at a height, z, is given by

$$p(z) = p_0 e^{\frac{-z}{H}}, \tag{11}$$

where H is the scale height, the distance over which the pressure falls by $1/e$. In the literature, 5 scale heights are often assumed for Δz for a clear atmosphere (at which point one is above 99.5% of the atmosphere), while 3 would be more reasonable in the moderately cloudy case (Puig et al. 2015; Tinetti et al. 2018; Edwards et al. 2019b). The scale height of the atmosphere is calculated from

$$H = \frac{kT_pN_A}{\mu g}, \tag{12}$$

where k is the Boltzmann constant, N_A is Avogadro's number, μ is the mean molecular weight of the atmosphere, and g is the surface gravity determined from

$$g = \frac{GM_p}{R_p^2}, \tag{13}$$

where M_p and R_p are the mass and radius of the planet, and G is the gravitational constant.

2.2.5. Eclipse Signal

During eclipse, the signal is calculated from two sources: reflected and emitted light from the planet. Emission from the exoplanet dayside is modeled as a blackbody, and the wavelength-dependent surface flux density is given by

$$S_p(\lambda, T_p) = \pi\frac{2hc^2}{\lambda^5}\frac{1}{e^{\frac{hc}{\lambda kT_p}} - 1}, \tag{14}$$

where T_p is the dayside temperature of the planet. The product of the blackbody emission and the solid angle subtended by the exoplanet at the telescope gives the spectral radiance at the aperture:

$$E_p^{\text{Emission}}(\lambda, T_p) = S_p(\lambda, T_p)\left(\frac{R_p}{d}\right)^2 \tag{15}$$

in W m^{-2} μm^{-1}. Additionally, a portion of the stellar light incident on the exoplanet is reflected. The strength of this reflected signal is strongly dependent on wavelength and can be significant at visible wavelengths. The flux of reflected light at the telescope aperture is calculated from

$$E_p^{\text{Reflection}}(\lambda) = \alpha_{\text{geom}}S_s(\lambda)\left(\frac{R_*}{d}\right)^2\left(\frac{R_p}{a}\right)^2, \tag{16}$$

where $S_S(\lambda)$ is the star spectral irradiance, a is the star–planet distance (i.e., the planet's semimajor axis), and α_{geom} is the geometric albedo, which is assumed to be that of a Lambertian sphere $\left(\frac{2}{3}\alpha_{\text{bond}}\right)$, wavelength independent, and at a phase of $\phi = 1$ (i.e., full-disk illumination).

2.2.6. Signal-to-noise Ratio

From these equations, and the error on the transit/eclipse depth, the signal-to-noise ratio (S/N) on the atmospheric signal can be obtained for a single observation. Assuming the S/N increases with the square root of the number of observations, the S/N after multiple transits/eclipses is given by

$$\text{S/N}_N = \sqrt{N}\,\text{S/N}_1, \tag{17}$$

where S/N_1 is the S/N of a single observation and N is the total number of observations. By setting a requirement on the S/N (S/N_R), the number of observations needed for a given planet can be ascertained from

$$N = \left(\frac{\text{S/N}_R}{\text{S/N}_1}\right)^2. \tag{18}$$

The current requirements are set to a median S/N > 7 across 1.0–4.5 μm for transit observations and 1.5–4.5 μm for eclipse measurements. In the former of these, the shorter wavelengths are excluded to avoid biasing against planets around cooler stars while the latter is chosen as planetary emission, even for relatively hot planets (~1500 K), is low at wavelengths shorter than 1.5 μm. Using Equation (18), one can then determine the type(s) of observation the planet is suited to.

2.3. Atmospheric Modeling

To simulate transmission (and emission) forward models, the open-source exoplanet atmospheric retrieval framework TauREx 3 (Waldmann et al. 2015a, 2015b; Al-Refaie et al. 2019) is used. Within TauREx 3, cross-section opacities are calculated from the ExoMol database (Yurchenko & Tennyson 2012) where available and from HITEMP (Rothman & Gordon 2014) and HITRAN (Gordon et al. 2016) otherwise. The H ion is included using the procedure outlined in John (1988) and Edwards et al. (2020). For atmospheric chemistry, two options are available within the Terminus infrastructure: chemical equilibrium, which is achieved using the ACE code (Agúndez et al. 2012; Venot et al. 2012) and takes the C/O ratio and metallicity as input, or free chemistry, which allows the user to choose molecules and their abundances. Alternatively, a high-resolution spectrum produced by another radiative transfer code can be read in or, if a retrieval on actual data has been performed, the atmosphere can be extrapolated from a TauREx 3 hdf5 file. Once the forward model is created at high resolution, it is then binned to the instrument resolution using TauREx 3's integrated binning function.

2.4. Light-curve Modeling and Fitting

For each spectral bin, PyLightCurve[4] (Tsiaras et al. 2016a) is used to model a noise-free transit/eclipse of the planet. The transits were all modeled with quadratic limb-darkening coefficients from Claret et al. (2013), calculated using ExoTETHyS (Morello et al. 2020). The Twinkle spectrometer features a split at 2.43 μm, creating two channels. For each of these, a white light curve is also generated. The spectral light curves are created at the native resolution of the instrument ($R \sim 20$–70). A time series is created with a cadence equal to the time between destructive reads and the light curve integrated over each of these exposures. The noise per integration, as calculated in Section 2.2, is then used to create noisy light curves by adding Gaussian scatter. Further updates will include the ability to add ramps due to detector persistence as well as other time-varying systematics.

For the fitting of the light curves, a Markov chain Monte Carlo (MCMC) is run using emcee (Foreman-Mackey et al. 2013) via the PyLightCurve package, here with 150,000

[4] https://github.com/ucl-exoplanets/pylightcurve

iterations, a burn-in of 100,000, and 100 walkers. For the simulations shown here, both white light curves are individually fitted with the inclination (i), reduced semimajor axis (a/R_*), transit midtime (T_0), and planet-to-star radius ratio (R_p/R_s) as free parameters. A weighted average of the recovered values for each of these parameters, except the planet-to-star radius ratio, is then fixed for the fitting of the spectral light curves where only the planet-to-star radius ratio is fitted. This provides a retrieved transit/eclipse depth for each light curve, along with the error associated with this parameter. If further complexity, such as ramps, is added to the light curve, future iterations of the code will allow for multiple light-curve fits. In this case, the uncertainties in the individual data points are increased such that their median matches the standard deviation of the residuals, a common technique when analyzing Hubble observations of exoplanets (e.g., Kreidberg et al. 2014; Tsiaras et al. 2016b).

For fainter targets, a spectrum with a reduced resolution can be requested and Terminus will combine the light curves and provide a spectrum with a resolution as close to the desired as possible. While the default cadence is set by the saturation time of the detector, it can be lowered or exposures can be combined. Additionally, multiple transits (or eclipses) can be individually modeled, fitted, and then combined. These functionalities are all controlled by the input configuration file. Once a spectrum has been generated, an automated interface with TauREx 3 can then be used to fit the data and retrieve the atmospheric parameters.

To compare the errors predicted by the radiometric model to those from fitted light curves, we model a single observation of HD 209458 b (Charbonneau et al. 2000; Henry et al. 2000). For the atmosphere, we model a composition based loosely on that retrieved from the HST data of this planet (Tsiaras et al. 2016b; MacDonald & Madhusudhan 2017). We assume a plane-parallel atmosphere with 100 layers and include the contributions of collision-induced absorption (CIA) of H_2–H_2 (Abel et al. 2011; Fletcher et al. 2018) and H_2–He (Abel et al. 2012), Rayleigh scattering, and gray clouds. In terms of molecular line lists, we import the following: H_2O (Polyansky et al. 2018), NH_3 (Yurchenko et al. 2011), CH_4 (Yurchenko et al. 2017), and HCN (Barber et al. 2014).

Figure 3 displays the errors on the transit depth predicted by the radiometric portion of Terminus as well as the uncertainties recovered from the light-curve fits. While the agreement is generally good, within 10%, there appears to be a wavelength-dependent effect on the accuracy of the radiometric tool. The trend seen could be due to the limb-darkening coefficients, which change with wavelength and alter the shape of the light curve.

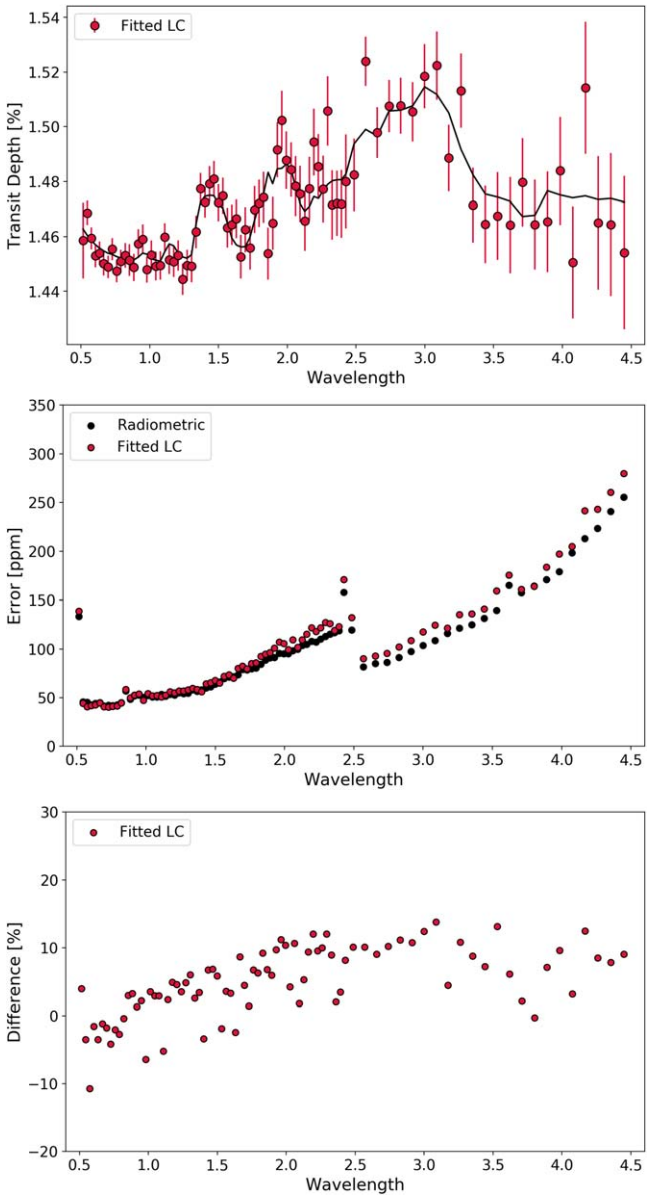

Figure 3. Comparison of error bars obtained from the radiometric model (black) and light-curve fitting for HD 209458 b. The wavelength-dependent difference between the models could be due to limb-darkening coefficients.

3. Orbit Modeling

Observatories in low-Earth orbits can experience interruptions in target visibility due to Earth occultations. Additionally, instruments and spacecraft usually have specific target–Sun, target–Moon, or target–Earth limb restrictions. To account for these, Terminus is capable of modeling the orbit of a spacecraft and calculating angles between the target and the Earth limb, the Sun, or other celestial body, in a similar way to tools used for other missions (e.g., for CHEOPS: Kuntzer et al. 2014).

The tool operates within an Earth-centered frame and the positions of celestial objects (the Sun, Moon, etc.) are loaded from the JPL Horizons service.[5] The spacecraft's orbit is defined by an ellipse that is subsequently inclined with respect to the X plane. The R.A. of the ascending node (RAAN) is then used to rotate this about the Z-axis.

Twinkle will operate in a Sun-synchronous orbit and here we modeled the following orbital parameters: altitude = 700 km, inclination = 90°.4, eccentricity = 0, RAAN = 190°.4 (i.e., 6 am). These are subject to change based upon launch availability but provide an approximate description of the expected operational state. The orbit of Twinkle during 2024 May is depicted in Figure 4.

As mentioned, the code can impose a number of exclusion angles to explore their effects on target availability. Here, we modeled the Sun, Earth, and Moon exclusion angles of 140°, 20°, and 5°, respectively. The first of these is largely due to thermal constraints while the latter two are to reduce stray light. The Earth and Moon exclusion angles for Twinkle are still under study but the values chosen here are similar to those of

[5] https://ssd.jpl.nasa.gov/horizons.cgi

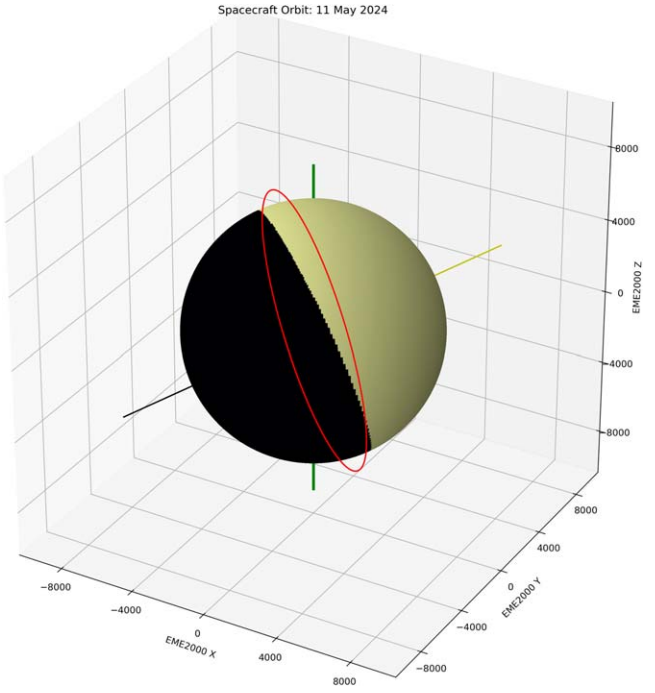

Figure 4. Modeled orbit of Twinkle (red) during 2024 May. The yellow vector indicates the direction of the Sun while the black one represents the anti-Sun vector (i.e., the center of Twinkle's field of regard). Earth is represented by the sphere with the terminator between day and night roughly shown.

other observatories operating in Sun-synchronous orbits or those proposed to do so (Deroo et al. 2012; Kuntzer et al. 2014).

The effects of each exclusion angle on the sky coverage are shown in Figure 5 along with the effect of combining them all. In each case, the metric shown is the total time the area of the sky can be observed over the course of a year. The plots highlight Twinkle's excellent coverage of the ecliptic plane although it, like CHEOPS, lacks the ability to study planets close to the ecliptic poles. However, the JWST and Ariel missions will prefer the polar regions, as shown in Figure 6, and thus both Twinkle and CHEOPS provide complementary coverage.

4. Partial Light Curves

From an exoplanet modeling perspective, it has thus far been assumed that a full light curve is observed. However, in reality, for space telescopes in a low-Earth orbit, sometimes only partial light curves will be obtained due to Earth obscuration as discussed in Section 3. These gaps cannot be completely accounted for in radiometric models, and thus a time-domain code, such as Terminus, is required.

To verify the orbital code created, and to explore the effect of partial light curves, we check our results against those of Edwards (2019). In Edwards (2019), the mission design, analysis, and operation software Freeflyer[6] was used to model the obscurations of HD 209458 b by Earth throughout a year. FreeFlyer has previously been used to support planning for several missions including NASA's Solar Dynamics Observatory (SDO). We note that Freeflyer only models the physical obscuration of the target star by Earth, and thus, for this comparison, we set the Earth exclusion angle to zero.

[6] https://ai-solutions.com/freeflyer/

As mentioned, Twinkle's field of regard means targets are not constantly observable, and in a year, 17 transits of HD 209458 b would be observable by Twinkle. Given the sky location of HD 209458, right ascension (R.A.): 330.°79; declination (decl.): 18.°88, the target will always be periodically obscured by Earth. In Figure 7, we show a comparison between the predicted gaps for the first of these transits, which are shown to be in excellent agreement. Meanwhile, Figure 8 displays the increase in gap size that would be incurred by various Earth exclusion angles. Going from an angle of 0° to 20° increases the gap size from 20 to 44 minutes. The latter case would mean Twinkle could be on target for over half an orbit (54 minutes). In comparison, past Hubble observations featured gaps of 47 minutes, with 48 minutes on target per orbit (Deming et al. 2013; Tsiaras et al. 2016b). Hence, Twinkle's observing efficiency for HD 209458 b will probably be similar to that of Hubble. All potential transit observations of HD 209458 b have gaps or a similar size (see Figure 9).

Here, we fit the first available light curve, and the recovered spectrum, and associated errors, is shown in Figure 10. As expected, the gaps increase the uncertainties on the recovered transit depth. Using Equations (5) and (8), one would expect the error to increase by 35% $\left(\sigma_p = \sigma_f \times \frac{1}{\sqrt{0.55}} = 1.347\sigma_f\right)$. We see an increase of 20%–40% and thus the radiometric model may also provide reasonable errors for partial light curves.

However, some planets may have more variable gaps, due to their location in the sky and a changing spacecraft–Earth–target geometry, and thus may be affected more significantly. For these planets, the scheduling of observations is likely to be highly important. Terminus is able to provide input into studies exploring the effects of partial light curves.

As an initial step to understanding the variability of Earth obscuration, we now model observations of WASP-127 b (Lam et al. 2017). WASP-127 is located such that Twinkle will potentially have a continuous, unobstructed view of the target during a transit (R.A.: 160.°56, decl.: −3.°84). However, some potential observations will incur Earth obscuration, and the amount of time lost will be dependent upon the Earth exclusion angle required. In the case of the 20° exclusion angle modeled here, Twinkle would have access to one complete transit (i.e., no gaps due to Earth obscuration) in 2024 as shown in Figure 11. The other available observation periods would incur interruption up to a maximum of 45 minutes over a 98 minute orbit. In the case of the Hubble observations of WASP-127 b (Skaf et al. 2020; Spake et al. 2021), the spacecraft could only be pointed at the target for 40 minutes per orbit (55 minute gaps). Hence, through careful selection of observing windows, the efficiency of Twinkle's observations of WASP-127 b could be far greater than that of Hubble's for this target.

To understand the impact of these gaps, we simulate a set of light curves for a single observation of WASP-127 b and compare the errors on the transit depths when gaps are induced. Again, we base the atmosphere on current observations that suggest a large water abundance and potentially the presence of FeH (Skaf et al. 2020), which we model using the line lists from Dulick et al. (2003), Wende et al. (2010).

The results of these fittings are shown in Figure 12. The full light curve again has a wavelength-dependent variation from the predicted radiometric errors, but this is again relatively small. As expected, the fitting of the partial light curve results

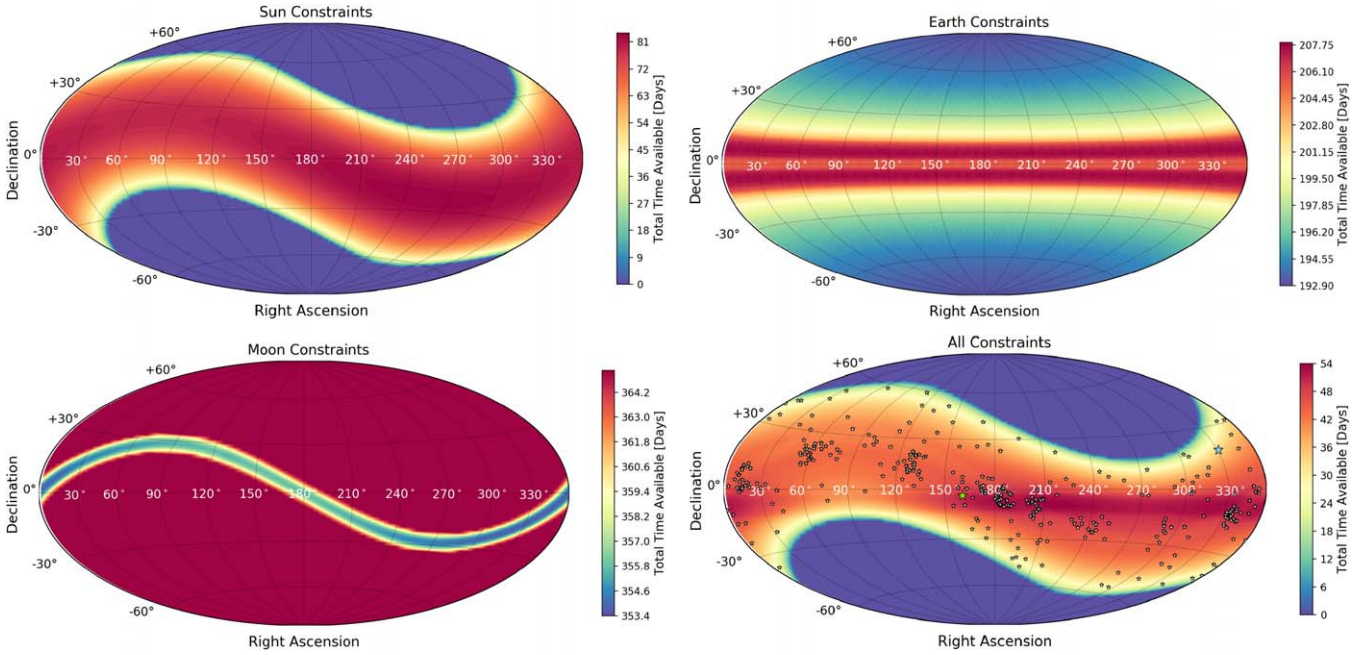

Figure 5. Sky coverage of Twinkle given the specific exclusion angles. The effects of individual constraints are shown for the Sun, Earth, and Moon alongside the combination of them all. Stars indicate known transiting exoplanet hosts, with HD 209458 and WASP-127 highlighted by light blue and green stars, respectively. We note that the color bar axes differ between each plot.

in larger uncertainties on the transit depth. In the case modeled, LC1 from Figure 11, Twinkle only observes the target for 46% of the transit. Using Equations (5) and (8), one would expect the error to increase by 48% $\left(\sigma_p = \sigma_f \times \frac{1}{\sqrt{0.46}} = 1.476\sigma_f\right)$. We see the increase is wavelength dependent and generally between 20% and 40%, less than predicted. Therefore, the radiometric model may not always be capable of providing accurate error estimations.

The recovered precision on different parameters is likely to be dependent upon the location of the gaps in the light curve. In this case, the central portion of the transit is well sampled, allowing for a precise recovery of the transit depth. However, ingress/egress are less well sampled, and thus orbital parameters such as the inclination (i) and reduced semimajor axis (a/R_*) may be less well determined.

Furthermore, the standard methodology of analyzing transiting exoplanet data is to fit to the light curves for planet-to-star radius ratio (R_p/R_s) to achieve a spectrum with error bars before performing atmospheric retrievals on the said spectrum. This approach, which has essentially been followed here, distills time-domain observations down to a single point and thus much information about the orbital parameters of the system are lost. Fitting of full light curves (no gaps) usually retrieves the orbital parameters accurately but, as discussed, gaps can lead to less certainty. This potential degeneracy is lost in the standard method and so, to bring the data analysis one step closer to the raw data, retrievals with Terminus-generated data could be conducted using the light curves themselves and the methodology described in Yip et al. (2020). The so-called "L-retrieval" allows for the orbital parameters (e.g., inclination, semimajor axis) to be free parameters in the retrieval to ensure that orbital degeneracies are accounted for. Such a methodology would be useful in the exploration of the effects of Earth obscuration, particularly as these orbital elements have been shown to be important in recovering the correct optical slope (Alexoudi et al. 2018). A thorough analysis is needed to explore this fully, and Terminus can feed vital information into such an effort.

5. Availability of Solar System Bodies

Twinkle will also conduct spectroscopy of objects within our solar system, with perhaps the most promising use of the mission in this regard being the characterization of small bodies. In particular, a diverse array of shapes for the 3 μm hydration feature, which generally cannot be observed from the ground, have been seen and used to classify asteroids (e.g., Mastrapa et al. 2009; Campins et al. 2010; Rivkin & Emery 2010; Takir & Emery 2012; Takir et al. 2013). Twinkle's broad wavelength coverage will allow for studies of this spectral feature, and many others, as outlined in Edwards et al. (2019a).

The times at which major and minor solar system bodies are within Twinkle's field of regard have previously been studied in Edwards et al. (2019a, 2019d). These studies showed that the outer planets, and main-belt asteroids, will have long, regular periods within Twinkle's field of regard. However, the observation periods of NEOs and near-Earth asteroids (NEAs) are far more sporadic. Hence, we revisit this analysis with the addition of considering Earth obscuration. For our example target, we choose 99942 Apophis (2004 MN4), a potentially hazardous asteroid (PHA). Apophis has a diameter of around 400 m (Müller et al. 2014; Licandro et al. 2015) and will have a close fly-by in 2029 (Figure 13). While it had been thought there was potentially a high probability of impact during this fly-by, or one in 2036, this has now been significantly downgraded (Chesley et al. 2010; Krolikowska & Sitarski 2010; Thuillot et al. 2015). Nevertheless, passing around 31,000 km from the Earth's surface, Apophis will come within the orbits of geosynchronous satellites (see Figure 13).

By comparing the data to likely meteorite analogs, current spectral analyses of Apophis have concluded it is an Sq-class asteroid that closely resembles the LL ordinary chondrite

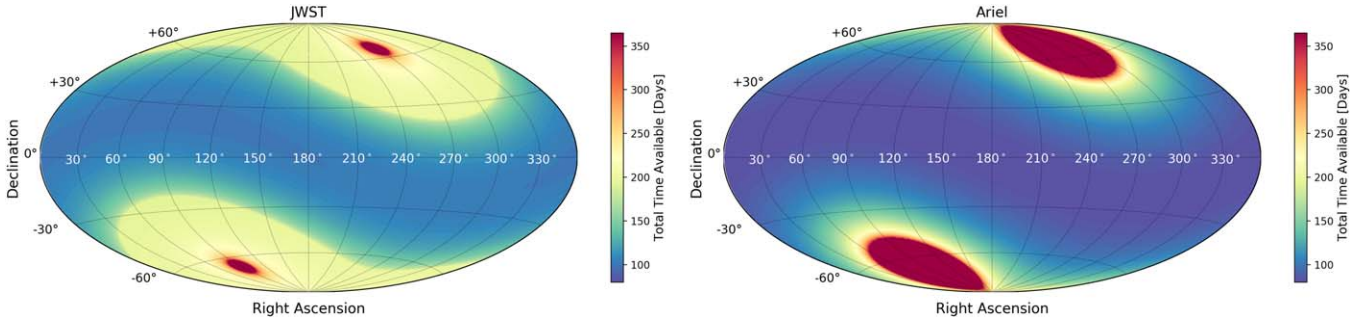

Figure 6. Sky coverage of JWST (left) and Ariel (right) which will have continuous viewing zones at the ecliptic poles. These missions are unaffected by Earth obscuration due to their L2 orbit.

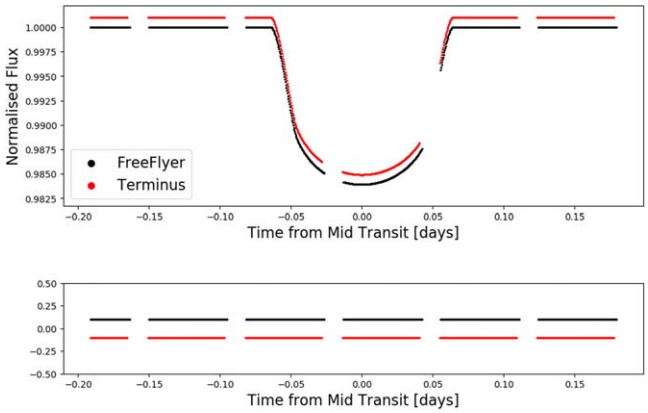

Figure 7. Comparison of the predicted gap sizes for HD 209458 b (R.A. = 330, decl. = 18) from Terminus and Freeflyer. The transit light curves are offset for clarity and the gap sizes are seen to be highly similar. We note that these gaps are due solely to physical obscuration by Earth, and no exclusion angle is included.

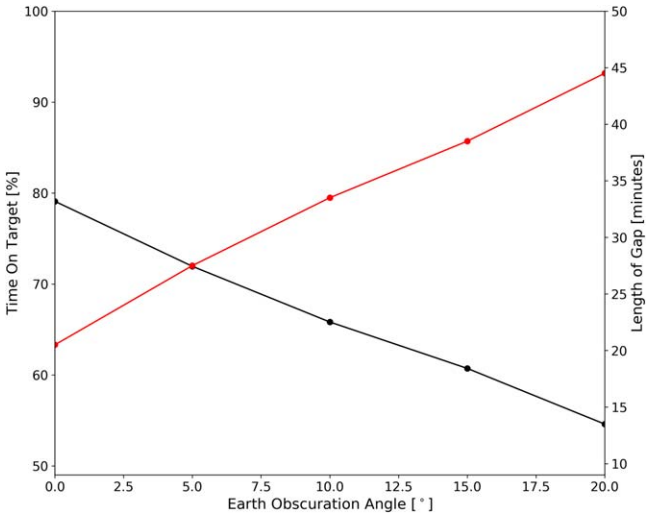

Figure 8. Effect of different Earth exclusion angles on the percentage of time on target (black) and the size of the gaps (red) for a transit observation of HD 209458 b.

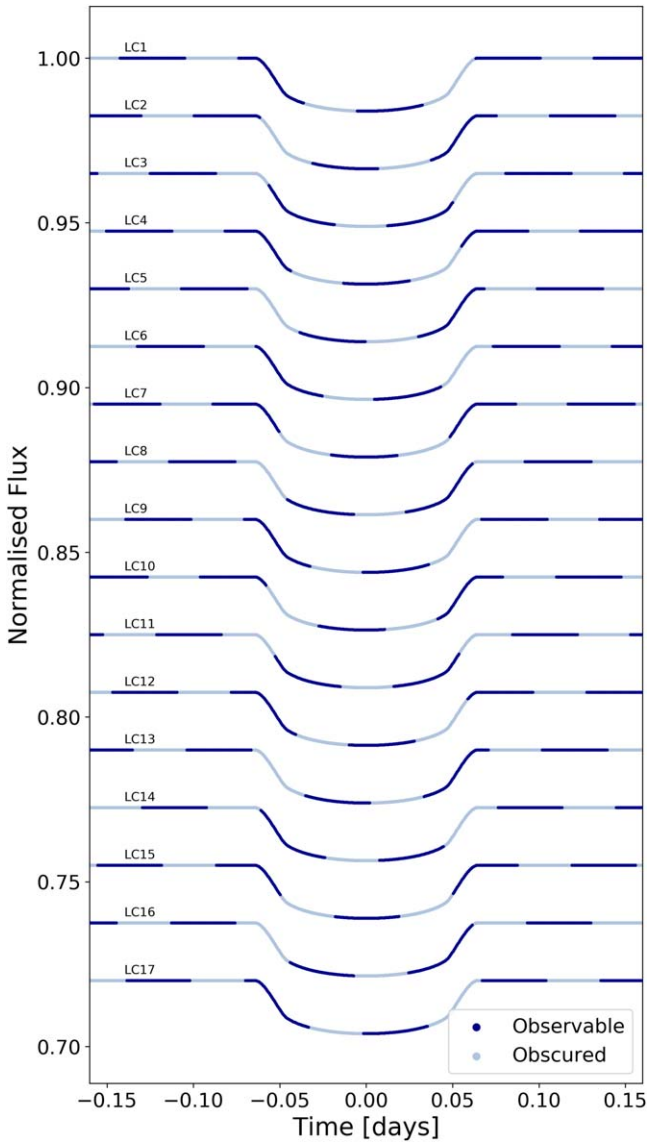

Figure 9. The 17 transits of HD 209458 b that are observable with Twinkle over the course of a single year. The gaps are due to Earth obscuration plus an exclusion angle of 20°. All light curves have gaps of roughly 45 minutes, which are comparable to those in the Hubble data of the same planet and have been offset for clarity.

meteorites in terms of composition (Binzel et al. 2009; Reddy et al. 2018). These data were measured over 0.55–2.45 μm, and similarities have been noted to that of the asteroid Itokawa, which was visited and studied by the Hayabusa mission (Abe et al. 2006).

Here, we analyze the availability of Apophis over the week before, and day after, its closest approach to Earth. Terminus obtains asteroid ephemerides using the astropy API to the JPL Horizons database (Astropy Collaboration et al. 2018). In Figure 14, we show the visible magnitude and apparent rate of motion of Apophis during this period. The interlaced dark and

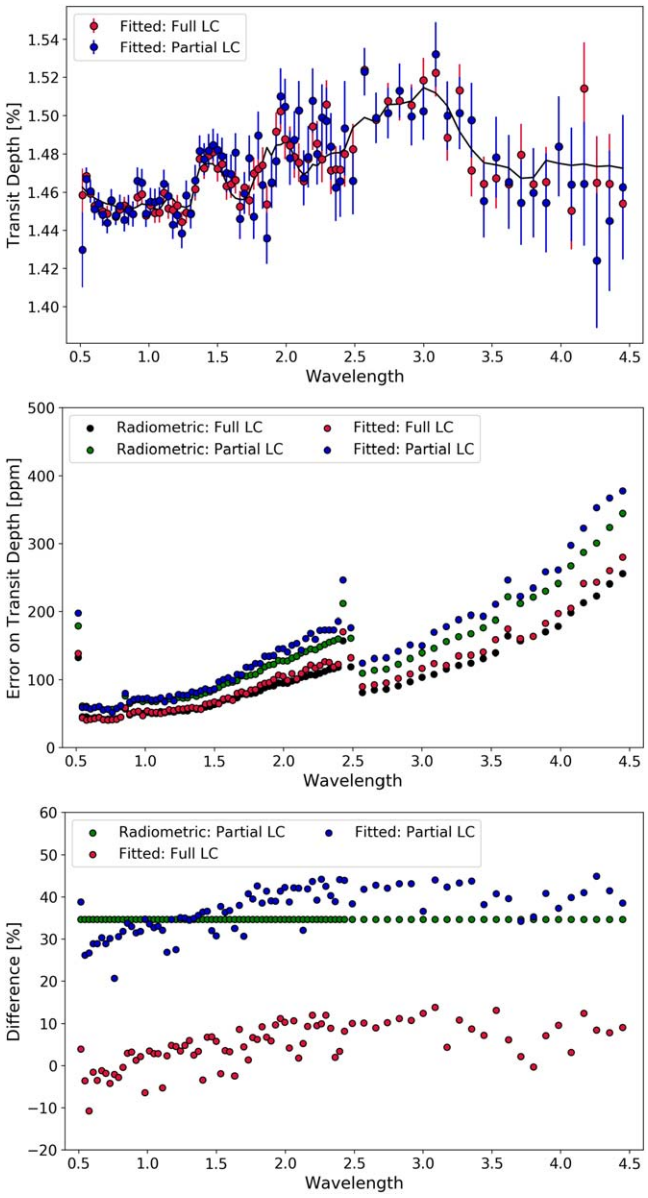

Figure 10. Recovered spectrum and error bars from different light-curve fits for HD 209458 b. In each case, red represents the fitting of a full light curve (same as Figure 3), blue the fitting of the partial light curve (LC1 from Figure 9), and black represents the predicted error from the radiometric model. The partial light curve results in far larger uncertainties due to the reduction in the number of data points.

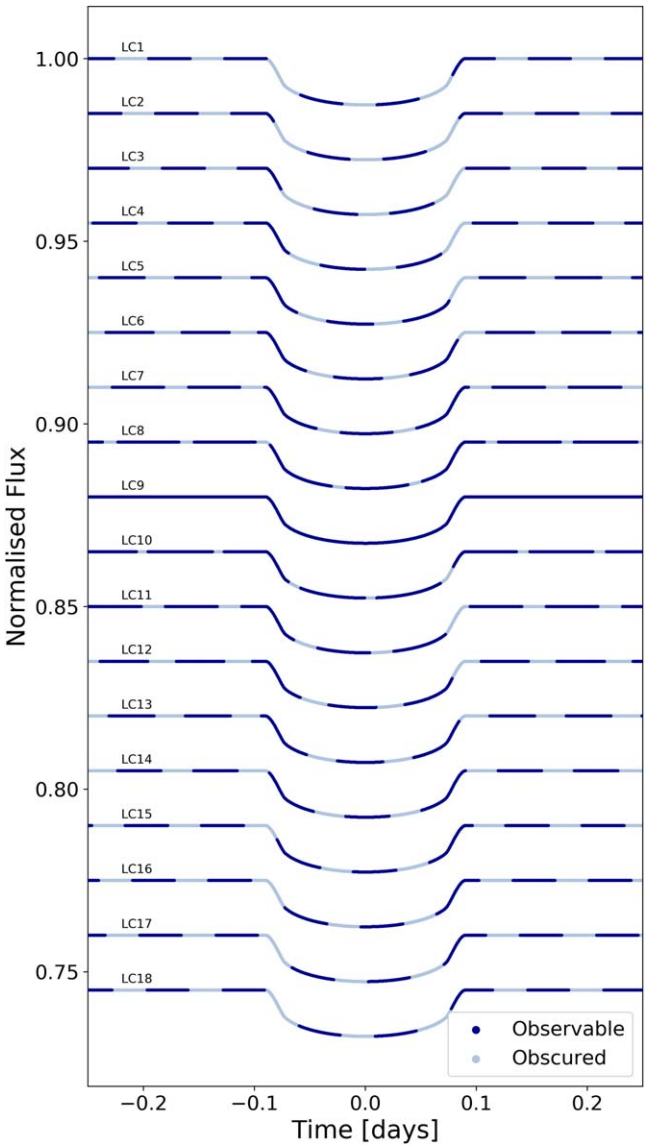

Figure 11. The 18 transits of WASP-127 b that are observable with Twinkle in 2024, which have been offset for clarity. The gaps are due to Earth obscuration plus an exclusion angle of 20°. LC 9 has no gaps, highlighting the importance of observational planning with Twinkle, or other low-Earth-orbit satellites, and the benefit of a Sun-synchronous orbit over the equatorial orbit of Hubble.

light blue segments show the availability of the asteroid before it leaves the field of regard soon after the closest point of its fly-by. The trajectory across the sky of Apophis is depicted in Figure 15 along with the sky coverage of Twinkle over this period.

The ability of spacecraft to accurately track nonsidereal objects is key for their observation. The Spitzer Space Telescope was used extensively for characterizing small bodies (e.g., Trilling et al. 2007; Barucci et al. 2008) and tracked objects moving at rates of 543 mas/s (Trilling et al. 2010). Spitzer was oriented using an inertial reference unit comprising of several high-performance star trackers and observed asteroids using linear track segments. These were commanded as a vector rate in J2000 coordinates, passing through a specified R.A. and decl. at a specified time. The coordinates of the target can be obtained from services such as the Jet Propulsion Laboratory's Horizons System. JWST is expected to be able to track objects moving at up to 30 mas/s (Thomas et al. 2016).

The maximum rate at which Twinkle can track nonsidereal objects is still under definition but will be >30 mas/s, which we take here as a conservative maximum value. When this threshold is crossed, Apophis will have a visible magnitude of approximately 11.8. During the day or so before this rate limit is crossed, Apophis would be available for periods of 55 minutes, with 40 minute interruptions, again assuming a 20° Earth exclusion angle.

As demonstrated in Figure 16, such observation windows provide plenty of time to achieve high-quality spectra. Here we simulated spectra for Apophis at a visible magnitude of 12 and an integration time of 5 minutes. We note that the thermal emission from the asteroid has been subtracted, which was modeled as a blackbody with a temperature of 300 K, to give

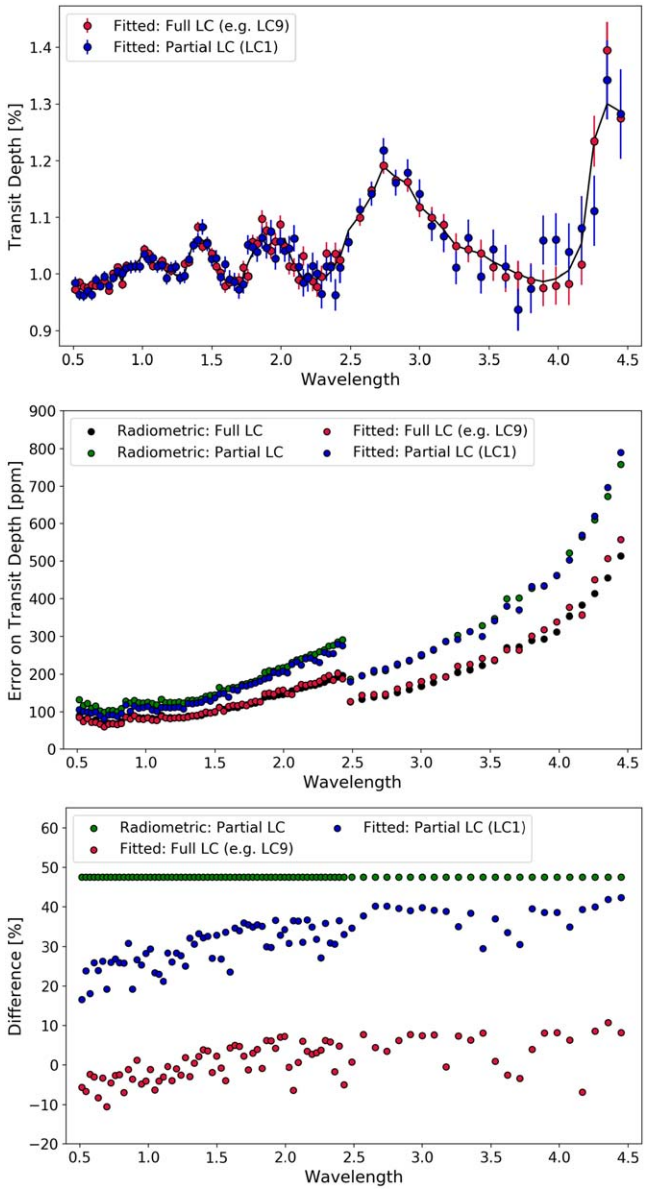

Figure 12. Recovered spectrum and error bars from different light-curve fits for WASP-127 b. In each case, red represents the fitting of a full light curve (e.g., LC9 in Figure 11), blue the fitting of the partial light curve (LC1 from Figure 11), and black represents the predicted error from the radiometric model. The errors from the full light curve are found to agree with the radiometric prediction, again with the exception of a slight, wavelength-dependent, variation. The partial light curve results in far larger uncertainties.

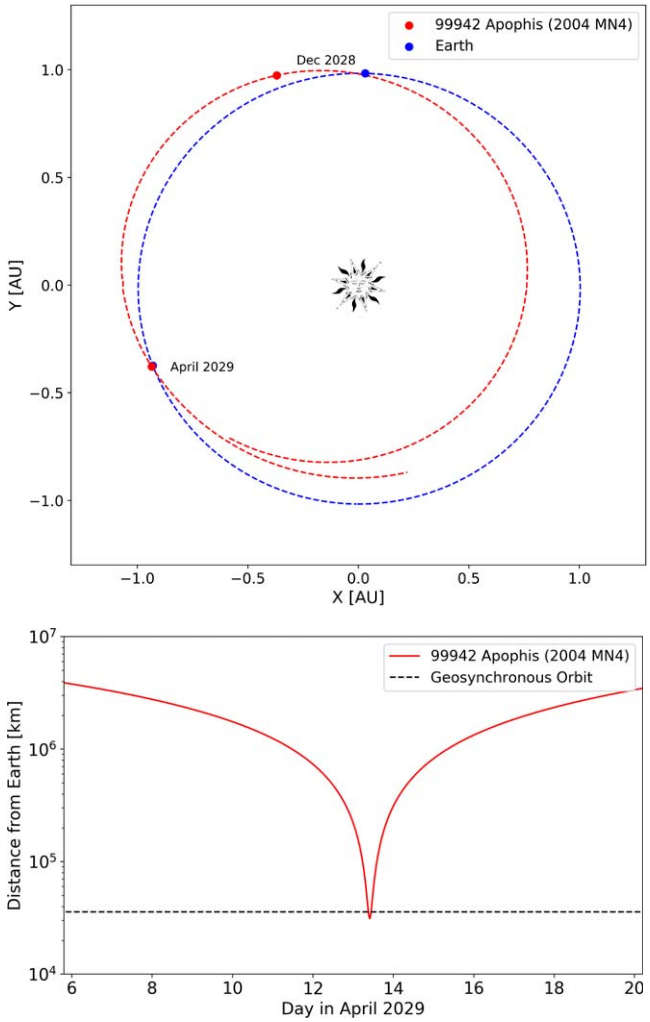

Figure 13. Top: orbit of Earth and Apophis from 2028 June to 2029 June. In the period, Apophis crosses the orbit of Earth twice with the second of these crosses occurring during 2029 April. Bottom: the distance between Earth and Apophis during 2029 April, highlighting that the minimum separation from the Earth surface is closer than geosynchronous satellites. Data for these plots were acquired via the NASA JPL Horizons service.

the relative reflectance of the asteroid. The input spectrum was taken from the RELAB database[7] and is of an LL6 ordinary chondrite meteorite.

Simulations have suggested the 2029 close encounter could cause landslides on Apophis, if the structure of some parts of the structure are significantly weak (Yu et al. 2014). The potential for resurfacing NEOs during terrestrial encounters is discussed in, e.g., Binzel et al. (2010) and Nesvorný et al. (2010), and spectral measurements can inform us on the freshness of the asteroid's surface, providing evidence for such mechanisms. Additionally, while an impact in 2029 has been ruled out, the potential for a future collision cannot be disregarded, and further study of the object is needed to refine this. In particular, the Yarkovsky effect has been shown to significantly alter predictions beyond 2029 and is sensitive to the physical parameters of Apophis, such as its albedo, diameter, and density (Farnocchia et al. 2013; Yu et al. 2017).

By observing Apophis simultaneously from 0.5–4.5 μm, Twinkle could significantly inform the debate surrounding the nature of Apophis, and its potential threat level to Earth. Therefore, Twinkle could have a role to play in characterizing known NEOs and NEAs, along with those predicted to be discovered by the Near-Earth Object Surveillance Mission (NEOSM; Mainzer et al. 2019) and the Vera C. Rubin Observatory, previously known as the Large Synoptic Survey Telescope (LSST; Jones et al. 2018). The ability of Twinkle to contribute to the study of NEOs and NEAs, and other specific asteroid populations, will be thoroughly detailed in further work.

6. Conclusions and Future Work

Terminus, a simulator with some time-domain capabilities, has been developed to model observations with space-based

[7] http://www.planetary.brown.edu/relab/

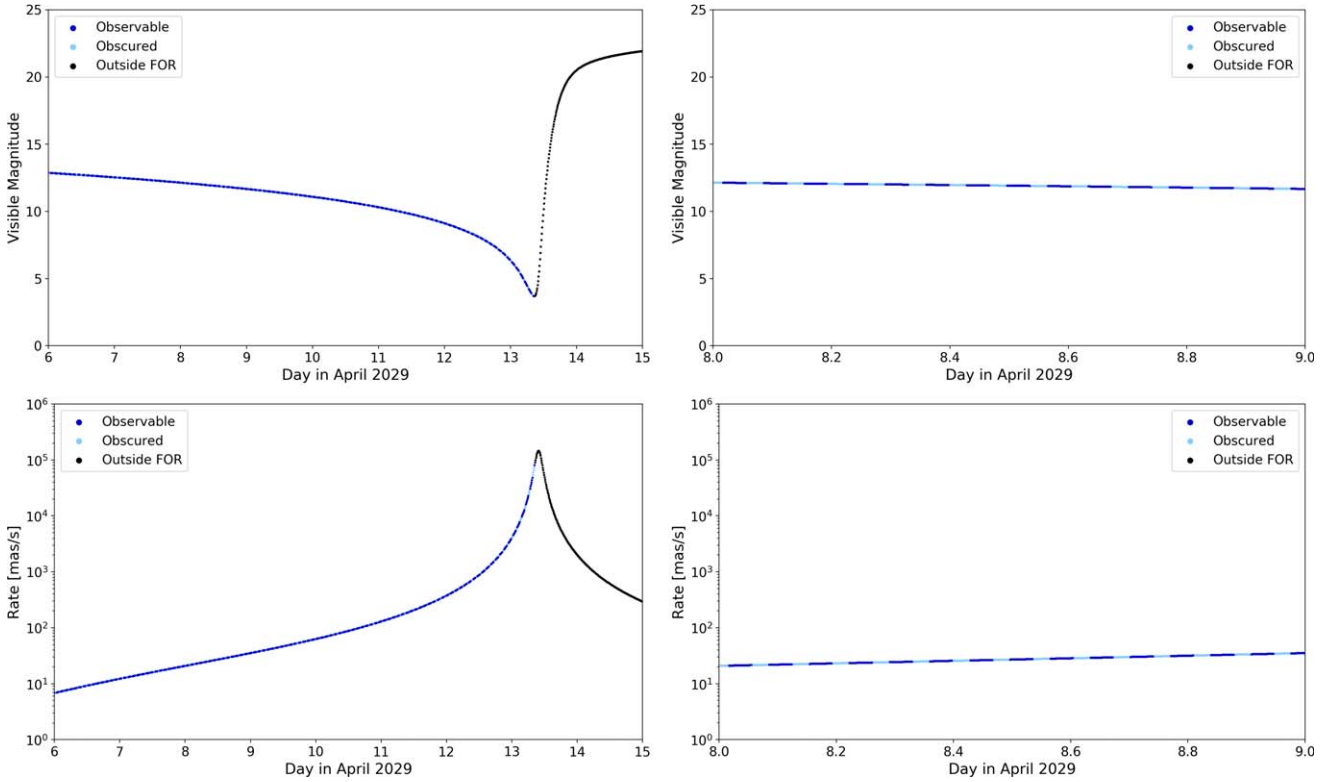

Figure 14. Visible magnitude (top) and rate of apparent motion (bottom) for Apophis during its close fly-by in 2029. The availability of Apophis was checked at a cadence of 1 minute with dark blue indicating it is unobstructed, light blue showing times at which Earth is occulting the target, and black representing the times when it has left the field of regard (i.e., exclusion due to Sun–target angle). The left-hand plots show these values for the week before the closest approach while the right-hand plots display the Earth obscuration more readily as Apophis approaches a rate of 30 mas/s.

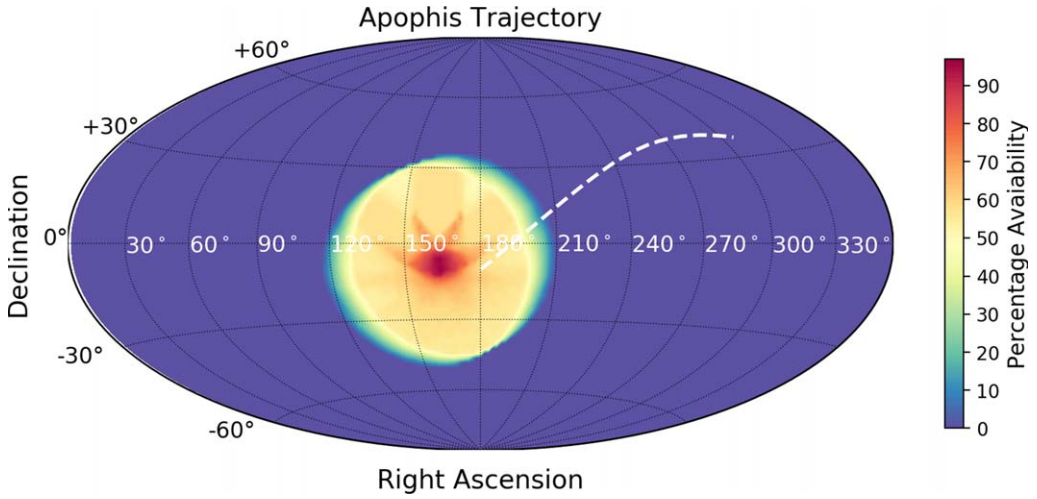

Figure 15. Average sky coverage during the two weeks before the closest approach of Apophis and the sky location of Apophis over that same period (white). It should be noted that, for the plotted Apophis trajectory, the time spent outside the FOR is only a few hours whereas the time spent within it equates to several days.

telescopes. This model is especially applicable to exoplanets and can incorporate gaps in the light curve, caused by Earth obscuration, and be used to predict the potential impact on the accuracy of the retrieved atmospheric composition. Here, Terminus is baselined on the Twinkle Space Telescope, but the model can be adapted for any space-based telescope and is especially applicable to those in a low-Earth orbit.

The impact of gaps in exoplanet observations has not been fully explored and further work is needed. Obtaining a full transit, or eclipse, light curve is obviously the ideal case but when it is not possible, such as for HD 209458 b, an optimization of the location, and length, of the gaps is required. By being able to model when these gaps occur, it should be possible to begin to explore this by running multiple fittings and comparing the retrieved transit depth and atmospheric parameters.

The Earth exclusion angle considered here is identical for the lit and unlit portions of Earth. However, each will contribute different amounts of stray light and thus likely have separate exclusion angles. Future work will incorporate this capability,

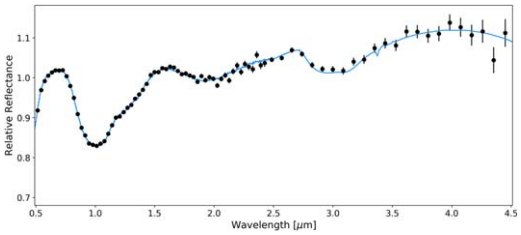

Figure 16. Simulated spectra for Apophis. The error bars are for a single exposure with a 300 s integration time on an object at a visible magnitude of 12. The spectrum is of an LL6 ordinary chondrite meteorite, taken from the RELAB database (bkr1dp015). We note that the reflectance shown here at shorter wavelengths (<0.8 μm) is slightly larger than found in actual studies of Apophis (Binzel et al. 2009; Reddy et al. 2018).

along with the capacity to quantitatively model the expected stray light from Earth and Moon to firmly establish the exclusion angles required. The effect of different orbital parameters (e.g., altitude, 6am versus 6pm RAAN) can also be explored. Terminus will be updated to include the South Atlantic Anomaly (SAA) to model the impact in the event that the spacecraft must limit scientific operations during its ingress into this region. Other additional development aspects include satellite ground stations and calculating potential accesses to these facilities. Such capabilities will allow for the tool to serve wider concept of operations (CONOPS) concerns and, in the event that spacecraft design for any reason limits operations during downlink, this can then be accounted for in the scheduling. Additionally, Terminus could also be used to model other effects such as stellar variability or detector ramps such as those seen on Hubble and Spitzer.

Finally, Terminus will be incorporated into a web interface to provide the community with simulations of Twinkle's capabilities. Doing so will allow the tool to be more widely used and facilitate in-depth studies of Twinkle's capabilities. These could include modeling various atmospheric scenarios for each planet to judge its suitability for characterization (e.g., Fortenbach & Dressing 2020), performing retrievals on populations of exoplanets (e.g., Changeat et al. 2020), classifying groups of planets via color–magnitude diagrams (e.g., Dransfield & Triaud 2020), testing machine-learning techniques for atmospheric retrieval (e.g., Márquez-Neila et al. 2018; Zingales & Waldmann 2018; Hayes et al. 2020; Yip et al. 2020), or the exploration of potential biases in current data analysis techniques (e.g., Feng et al. 2016; Rocchetto et al. 2016; Caldas et al. 2019; Changeat et al. 2019; Powell et al. 2019; MacDonald et al. 2020; Taylor et al. 2020). Additionally, thorough analyses of Twinkle's capabilities for specific scientific endeavors, such as confirming/refuting the presence of thermal inversions and identifying optical absorbers in ultrahot Jupiters (e.g., Fortney et al. 2008; Spiegel et al. 2009; Haynes et al. 2015; Evans et al. 2018; Parmentier et al. 2018; Edwards et al. 2020; Pluriel et al. 2020; von Essen et al. 2020; Changeat & Edwards 2021), searching for an exoplanet mass–metallicity trend (e.g., Wakeford et al. 2017; Welbanks et al. 2019), probing the atmospheres of planets in/close to the radius valley to discern their true nature (e.g., Owen & Wu 2017; Fulton & Petigura 2018; Zeng et al. 2019), refining basic planetary and orbital characteristics (e.g., Berardo et al. 2019; Dalba & Tamburo 2019; Livingston et al. 2019), measuring planet masses through accurate transit timings (e.g., Hadden & Lithwick 2017; Grimm et al. 2018; Petigura et al. 2018), verifying additional planets within systems (e.g., Gillon et al. 2017; Bonfanti et al. 2021), studying nontransiting planets by measuring the planetary infrared excess (Stevenson 2020), or even contributing to the search for exomoon candidates (e.g., Simon et al. 2015; Heller et al. 2016; Teachey & Kipping 2018), can also be undertaken.

This work has utilized data from FreeFlyer, a mission design, analysis, and operation software created by a.i. solutions. We thank Giovanna Tinetti, Marcell Tessenyi, Giorgio Savini, Subhajit Sarkar, Enzo Pascale, Angelos Tsiaras, Philip Windred, Andy Rivkin, Lorenzo V. Mugnai, Kai Hou Yip, Ahmed Al-Refaie, Quentin Changeat, and Lara Ainsman for their guidance, comments, and useful discussions. This work has been partially funded by the STFC grant ST/T001836/1 and by the UKSA grant ST/V003380/1.

Software: TauREx 3 (Al-Refaie et al. 2019), pylightcurve (Tsiaras et al. 2016a), ExoTETHyS (Morello et al. 2020), ExoSim (Sarkar et al. 2020b), Astropy (Astropy Collaboration et al. 2018), h5py (Collette 2013), emcee (Foreman-Mackey et al. 2013), Matplotlib (Hunter 2007), Multinest (Feroz et al. 2009; Buchner et al. 2014), Pandas (Reback et al. 2020), Numpy (Oliphant 2006), SciPy (Virtanen et al. 2020), corner (Foreman-Mackey 2016).

ORCID iDs

Billy Edwards https://orcid.org/0000-0002-5494-3237

References

Abe, M., Takagi, Y., Kitazato, K., et al. 2006, Sci, 312, 1334
Abel, M., Frommhold, L., Li, X., & Hunt, K. L. 2011, JPCA, 115, 6805
Abel, M., Frommhold, L., Li, X., & Hunt, K. L. 2012, JChPh, 136, 044319
Agúndez, M., Venot, O., Iro, N., et al. 2012, A&A, 548, A73
Akeson, R. L., Chen, X., Ciardi, D., et al. 2013, PASP, 125, 989
Alexoudi, X., Mallonn, M., von Essen, C., et al. 2018, A&A, 620, A142
Allard, F., Homeier, D., & Freytag, B. 2012, RSPTA, 370, 2765
Al-Refaie, A. F., Changeat, Q., Waldmann, I. P., & Tinetti, G. 2019, arXiv:1912.07759
Astropy Collaboration, Price-Whelan, A. M., Sipőcz, B. M., et al. 2018, AJ, 156, 123
Baraffe, I., Homeier, D., Allard, F., & Chabrier, G. 2015, A&A, 577, A42
Barber, R. J., Strange, J. K., Hill, C., et al. 2014, MNRAS, 437, 1828
Barclay, T., Pepper, J., & Quintana, E. V. 2018, ApJS, 239, 2
Barucci, M., Fornasier, S., Dotto, E., et al. 2008, A&A, 477, 665
Batalha, N. E., Mandell, A., Pontoppidan, K., et al. 2017, PASP, 129, 064501
Benz, W., Broeg, C., Fortier, A., et al. 2021, ExA, 51, 109
Berardo, D., Crossfield, I. J. M., Werner, M., et al. 2019, AJ, 157, 185
Binzel, R. P., Morbidelli, A., Merouane, S., et al. 2010, Natur, 463, 331
Binzel, R. P., Rivkin, A. S., Thomas, C. A., et al. 2009, Icar, 200, 480
Bonfanti, A., Delrez, L., Hooton, M. J., et al. 2021, A&A, 646, A157
Bordé, P., Rouan, D., & Léger, A. 2003, A&A, 405, 1137
Buchner, J., Georgakakis, A., Nandra, K., et al. 2014, A&A, 564, A125
Caldas, A., Leconte, J., Selsis, F., et al. 2019, A&A, 623, A161
Campins, H., Hargrove, K., Pinilla-Alonso, N., et al. 2010, Natur, 464, 1320
Changeat, Q., Al-Refaie, A., Mugnai, L. V., et al. 2020, AJ, 160, 80
Changeat, Q., & Edwards, B. 2021, ApJL, 907, L22
Changeat, Q., Edwards, B., Waldmann, I. P., & Tinetti, G. 2019, ApJ, 886, 39
Charbonneau, D., Brown, T. M., Latham, D. W., & Mayor, M. 2000, ApJL, 529, L45
Chesley, S. R., Baer, J., & Monet, D. G. 2010, Icar, 210, 158
Claret, A., Hauschildt, P. H., & Witte, S. 2013, A&A, 552, A16
Collette, A. 2013, Python and HDF5 (Sebastopol, CA: O'Reilly Media Inc.)
Dalba, P. A., & Tamburo, P. 2019, ApJL, 873, L17
Deming, D., Wilkins, A., McCullough, P., et al. 2013, ApJ, 774, 95
Deroo, P., Swain, M. R., & Green, R. O. 2012, Proc. SPIE, 8442, 844241
Dransfield, G., & Triaud, A. H. M. J. 2020, MNRAS, 499, 505
Dulick, M., Bauschlicher, C. W., Jr., & Burrows, A. 2003, ApJ, 594, 651
Edwards, B. 2019, PhD thesis (Univ. College London)
Edwards, B., Changeat, Q., Baeyens, R., et al. 2020, AJ, 160, 8
Edwards, B., Lindsay, S., Savini, G., et al. 2019a, JATIS, 5, 034004
Edwards, B., Mugnai, L., Tinetti, G., Pascale, E., & Sarkar, S. 2019b, AJ, 157, 242
Edwards, B., Rice, M., Zingales, T., et al. 2019c, ExA, 47, 29

Edwards, B., Savini, G., Tinetti, G., et al. 2019d, JATIS, 5, 014006
Ehrenreich, D., Lovis, C., Allart, R., et al. 2020, Natur, 580, 597
Evans, T. M., Sing, D. K., Goyal, J. M., et al. 2018, AJ, 156, 283
Farnocchia, D., Chesley, S. R., Chodas, P. W., et al. 2013, Icar, 224, 192
Feng, Y. K., Line, M. R., Fortney, J. J., et al. 2016, ApJ, 829, 52
Feroz, F., Hobson, M. P., & Bridges, M. 2009, MNRAS, 398, 1601
Fletcher, L. N., Gustafsson, M., & Orton, G. S. 2018, ApJS, 235, 24
Focardi, M., Pace, E., Farina, M., et al. 2018, ExA, 46, 1
Foreman-Mackey, D. 2016, JOSS, 1, 24
Foreman-Mackey, D., Hogg, D. W., Lang, D., & Goodman, J. 2013, PASP, 125, 306
Fortenbach, C. D., & Dressing, C. D. 2020, PASP, 132, 054501
Fortney, J. J., Lodders, K., Marley, M. S., & Freedman, R. S. 2008, ApJ, 678, 1419
Fulton, B. J., & Petigura, E. A. 2018, AJ, 156, 264
Futyan, D., Fortier, A., Beck, M., et al. 2020, A&A, 635, A23
Garhart, E., Deming, D., Mandell, A., et al. 2020, AJ, 159, 137
Geers, V. C., Klaassen, P. D., & Beard, S. 2019, in ASP Conf. Ser. 523, Astronomical Data Analysis Software and Systems XXVII, ed. P. J. Teuben et al. (San Francisco, CA: ASP), 641
Gillon, M., Triaud, A. H. M. J., Demory, B.-O., et al. 2017, Natur, 542, 456
Gordon, I., Rothman, L. S., Wilzewski, J. S., et al. 2016, AAS/DPS Meeting, 48, 421.13
Greene, T. P., Line, M. R., Montero, C., et al. 2016, ApJ, 817, 17
Grimm, S. L., Demory, B.-O., Gillon, M., et al. 2018, A&A, 613, A68
Hadden, S., & Lithwick, Y. 2017, AJ, 154, 5
Hayes, J. J. C., Kerins, E., Awiphan, S., et al. 2020, MNRAS, 494, 4492
Haynes, K., Mandell, A. M., Madhusudhan, N., Deming, D., & Knutson, H. 2015, ApJ, 806, 146
Heller, R., Hippke, M., Placek, B., Angerhausen, D., & Agol, E. 2016, A&A, 591, A67
Henry, G. W., Marcy, G. W., Butler, R. P., & Vogt, S. S. 2000, ApJL, 529, L41
Hoeijmakers, H. J., Ehrenreich, D., Heng, K., et al. 2018, Natur, 560, 453
Hunter, J. D. 2007, CSE, 9, 90
Husser, T.-O., Wende-von Berg, S., Dreizler, S., et al. 2013, A&A, 553, A6
Iyer, A. R., Swain, M. R., Zellem, R. T., et al. 2016, ApJ, 823, 109
James, J. F., Mukai, T., Watanabe, T., Ishiguro, M., & Nakamura, R. 1997, MNRAS, 288, 1022
John, T. L. 1988, A&A, 193, 189
Jones, R. L., Slater, C. T., Moeyens, J., et al. 2018, Icar, 303, 181
Kreidberg, L., Bean, J. L., Désert, J.-M., et al. 2014, Natur, 505, 69
Krolikowska, M., & Sitarski, G. 2010, arXiv:1009.2639
Kuntzer, T., Fortier, A., & Benz, W. 2014, Proc. SPIE, 9149, 91490W
Lam, K. W. F., Faedi, F., Brown, D. J. A., et al. 2017, A&A, 599, A3
Leinert, C., Bowyer, S., Haikala, L. K., et al. 1998, A&AS, 127, 1
Licandro, J., Müller, T., Alvarez, C., Alí-Lagoa, V., & Delbò, M. 2015, arXiv:1510.06248
Livingston, J. H., Crossfield, I. J. M., Werner, M. W., et al. 2019, AJ, 157, 102
MacDonald, R. J., Goyal, J. M., & Lewis, N. K. 2020, ApJL, 893, L43
MacDonald, R. J., & Madhusudhan, N. 2017, MNRAS, 469, 1979
Mainzer, A., Bauer, J., Cutri, R., et al. 2019, EPSC-DPS Joint Meeting, 2019, EPSC–DPS2019–1049
Mainzer, A., Bauer, J., Cutri, R. M., et al. 2014, ApJ, 792, 30
Márquez-Neila, P., Fisher, C., Sznitman, R., & Heng, K. 2018, NatAs, 2, 719
Martin-Lagarde, M., Lagage, P.-O., Gastaud, R., et al. 2021, JOSS, 6, 2287
Mastrapa, R., Sandford, S., Roush, T., Cruikshank, D., & Dalle Ore, C. 2009, ApJ, 701, 1347
Morello, G., Claret, A., Martin-Lagarde, M., et al. 2020, AJ, 159, 75
Mugnai, L. V., Pascale, E., Edwards, B., Papageorgiou, A., & Sarkar, S. 2020, ExA, 50, 303
Müller, T. G., Kiss, C., Scheirich, P., et al. 2014, A&A, 566, A22
Murakami, H., Baba, H., Barthel, P., et al. 2007, PASJ, 59, S369
Nagler, P. C., Edwards, B., Kilpatrick, B., et al. 2019, JAI, 8, 1950011
Nesvorný, D., Bottke, W. F., Vokrouhlický, D., Chapman, C. R., & Rafkin, S. 2010, Icar, 209, 510
Nielsen, L. D., Ferruit, P., Giardino, G., et al. 2016, Proc. SPIE, 9904, 99043O
Oliphant, T. E. 2006, A Guide to NumPy, Vol. 1 (Spanish Fork, UT: Trelgol Publishing)
Owen, J. E., & Wu, Y. 2017, ApJ, 847, 29
Parmentier, V., Line, M. R., Bean, J. L., et al. 2018, A&A, 617, A110
Pascale, E., Waldmann, I. P., MacTavish, C. J., et al. 2015, ExA, 40, 601
Petigura, E. A., Benneke, B., Batygin, K., et al. 2018, AJ, 156, 89
Pluriel, W., Whiteford, N., Edwards, B., et al. 2020, AJ, 160, 112
Polyansky, O. L., Kyuberis, A. A., Zobov, N. F., et al. 2018, MNRAS, 480, 2597
Pontoppidan, K. M., Pickering, T. E., Laidler, V. G., et al. 2016, Proc. SPIE, 9910, 991016
Powell, D., Louden, T., Kreidberg, L., et al. 2019, ApJ, 887, 170
Puig, L., Isaak, K., Linder, M., et al. 2015, ExA, 40, 393
Puig, L., Pilbratt, G., Heske, A., et al. 2018, ExA, 46, 211
Rauscher, B. J., Fox, O., Ferruit, P., et al. 2007, PASP, 119, 7786
Reback, J., McKinney, W., Mendel, B., et al. 2020, pandas-dev/pandas: Pandas 1.0.3, v1.0.3, Zenodo doi:10.5281/zenodo.3715232
Reddy, V., Sanchez, J. A., Furfaro, R., et al. 2018, AJ, 155, 140
Ricker, G. R., Winn, J. N., Vanderspek, R., et al. 2014, Proc. SPIE, 9143, 914320
Rivkin, A., & Emery, J. 2010, Natur, 464, 1322
Rocchetto, M., Waldmann, I. P., Venot, O., Lagage, P. O., & Tinetti, G. 2016, ApJ, 833, 120
Rothman, L. S., & Gordon, I. E. 2014, Status of the HITRAN and HITEMP Databases, Zenodo, doi:10.5281/zenodo.11207
Sarkar, S., Madhusudhan, N., & Papageorgiou, A. 2020a, MNRAS, 491, 378
Sarkar, S., Papageorgiou, A., & Pascale, E. 2016, Proc. SPIE, 9904, 99043R
Sarkar, S., Papageorgiou, A., Tsikrikonis, I. A., Vandenbussche, B., & Pascale, E. 2017, ARIEL Performance Analysis Rep. ARIEL-CRDF-PL-AN-001
Sarkar, S., Pascale, E., Papageorgiou, A., Johnson, L. J., & Waldmann, I. 2020b, arXiv:2002.03739
Savini, G., Tessenyi, M., Tinetti, G., et al. 2018, Proc. SPIE, 9904, 99044M
Simon, A. E., Szabó, G. M., Kiss, L. L., Fortier, A., & Benz, W. 2015, PASP, 127, 1084
Sing, D. K., Fortney, J. J., Nikolov, N., et al. 2016, Natur, 529, 59
Skaf, N., Fabienne Bieger, M., Edwards, B., et al. 2020, AJ, 160, 109
Spake, J. J., Sing, D. K., Wakeford, H. R., et al. 2021, MNRAS, 500, 4042
Spiegel, D. S., Silverio, K., & Burrows, A. 2009, ApJ, 699, 1487
Sreejith, A. G., Fossati, L., Fleming, B. T., et al. 2019, JATIS, 5, 018004
Stevenson, K. B. 2020, ApJL, 898, L35
Takir, D., & Emery, J. 2012, Icar, 219, 641
Takir, D., Emery, J., McSween, H., et al. 2013, M&PS, 48, 1618
Taylor, J., Parmentier, V., Irwin, P. G. J., et al. 2020, MNRAS, 493, 4342
Teachey, A., & Kipping, D. M. 2018, SciA, 4, eaav1784
Thomas, C., Abell, P., Castillo-Rogez, J., et al. 2016, PASP, 128, 018002
Thuillot, W., Bancelin, D., Ivantsov, A., et al. 2015, A&A, 583, A59
Tinetti, G., Beaulieu, J. P., Henning, T., et al. 2012, ExA, 34, 311
Tinetti, G., Drossart, P., Eccleston, P., et al. 2018, ExA, 46, 135
Tinetti, G., Eccleston, P., Haswell, C., et al. 2021, arXiv:2104.04824
Trilling, D., Bhattacharya, B., Blaylock, M., et al. 2007, AAS DPS Meeting, 39, 484
Trilling, D., Mueller, M., Hora, J., et al. 2010, arXiv:1007.1009
Tsiaras, A., Waldmann, I., Rocchetto, M., et al. 2016a, pylightcurve: Exoplanet lightcurve model, Astrophysics Source Code Library, ascl:1612.018
Tsiaras, A., Waldmann, I. P., Rocchetto, M., et al. 2016b, ApJ, 832, 202
Tsiaras, A., Waldmann, I. P., Zingales, T., et al. 2018, AJ, 155, 156
Tsumura, K., Battle, J., Bock, J., et al. 2010, ApJ, 719, 394
Tucker, G. S., Nagler, P., Butler, N., et al. 2018, Proc. SPIE, 10702, 107025G
Varley, R., Tsiaras, A., & Karpouzas, K. 2017, ApJS, 231, 13
Venot, O., Hébrard, E., Agúndez, M., et al. 2012, A&A, 546, A43
Virtanen, P., Gommers, R., Oliphant, T. E., et al. 2020, NatMe, 17, 261
von Essen, C., Mallonn, M., Hermansen, S., et al. 2020, A&A, 637, A76
Wakeford, H. R., Sing, D. K., Kataria, T., et al. 2017, Sci, 356, 628
Waldmann, I. P., Rocchetto, M., Tinetti, G., et al. 2015a, ApJ, 813, 13
Waldmann, I. P., Tinetti, G., Rocchetto, M., et al. 2015b, ApJ, 802, 107
Welbanks, L., Madhusudhan, N., Allard, N. F., et al. 2019, ApJL, 887, L20
Wende, S., Reiners, A., Seifahrt, A., & Bernath, P. F. 2010, A&A, 523, A58
Werner, M. W., Roellig, T. L., Low, F. J., et al. 2004, ApJS, 154, 1
Wright, E. L., Eisenhardt, P. R. M., Mainzer, A. K., et al. 2010, AJ, 140, 1868
Yip, K. H., Changeat, Q., Nikolaou, N., et al. 2020, arXiv:2011.11284
Yip, K. H., Tsiaras, A., Waldmann, I. P., & Tinetti, G. 2020, AJ, 160, 171
Yu, L.-L., Ji, J., & Ip, W.-H. 2017, RAA, 17, 070
Yu, Y., Richardson, D. C., Michel, P., Schwartz, S. R., & Ballouz, R.-L. 2014, Icar, 242, 82
Yurchenko, S. N., Amundsen, D. S., Tennyson, J., & Waldmann, I. P. 2017, A&A, 605, A95
Yurchenko, S. N., Barber, R. J., & Tennyson, J. 2011, MNRAS, 413, 1828
Yurchenko, S. N., & Tennyson, J. 2012, EAS Pub. Ser., 58, 243
Zeng, L., Jacobsen, S. B., Sasselov, D. D., et al. 2019, PNAS, 116, 9723
Zingales, T., & Waldmann, I. P. 2018, AJ, 156, 268